Nanopatterning reconfigurable magnetic landscapes via thermally assisted scanning probe lithography

NATURE NANOTECHNOLOGY
Volume: 11 Issue: 6 Page: 545
DOI: 10.1038/NNANO.2016.25
Published: JUN 2016

E. Albisetti[1,2,*], D. Petti[1], M. Pancaldi[3], M. Madami[4], S. Tacchi[5], J. Curtis[2], W.P. King[6], A. Papp[7], G. Csaba[7], W.Porod[7], P. Vavassori[3,8], E. Riedo[2,9,*], R. Bertacco[1,10,*]

[1]Dipartimento di Fisica, Politecnico di Milano, 20133 Milano, Italy.

[2]School of Physics, Georgia Institute of Technology, Atlanta, GA 30332, USA.

[3]CIC nanoGUNE, E-20018 Donostia-San Sebastian, Spain.

[4]Dipartimento di Fisica e Geologia, Università di Perugia, Italy.

[5]Istituto Officina dei Materiali del CNR (CNR-IOM), Unità di Perugia, c/o Dipartimento di Fisica e Geologia, Perugia, Italy.

[6]Department of Mechanical Science and Engineering, University of Illinois Urbana-Champaign, Urbana, IL 61801, USA.

[7]Center for Nano Science and Technology, University of Notre Dame, Notre Dame, IN, 46556 USA.

[8]IKERBASQUE, Basque Foundation for Science, 48011, Bilbao, Spain.

[9]CUNY-Advanced Science Research Center and City College New York, City University of New York, 85 St Nicholas Terrace, New York, New York 10031, USA.

[10]IFN-CNR, c/o Politecnico di Milano, 20133 Milano, Italy.

*Correspondence to: edoardo.albisetti@polimi.it; elisa.riedo@asrc.cuny.edu;

riccardo.bertacco@polimi.it;

Abstract

The search for novel tools for controlling magnetism at the nanoscale is crucial for the development of new paradigms in optics, electronics and spintronics. So far, the fabrication of magnetic nanostructures has been mainly achieved through irreversible structural or chemical modifications. Here, we propose a new concept for creating reconfigurable magnetic nanopatterns, by crafting at the nanoscale the magnetic anisotropy landscape of a ferromagnetic layer exchange-coupled to an antiferromagnetic one. By performing a localized field cooling with the hot tip of a scanning probe microscope, magnetic structures, with arbitrarily oriented magnetization and tunable unidirectional anisotropy, are reversibly patterned without modifying the film chemistry and topography. This opens unforeseen possibilities for the development of novel metamaterials with finely tuned magnetic properties, such as reconfigurable magnetoplasmonic and magnonic crystals. In this context, we experimentally demonstrate the spatially controlled spin-waves excitation and propagation in magnetic structures patterned with the proposed method.

Metamaterials are composite materials in which new functionalities emerge from engineered combinations of carefully chosen and nanoscale designed material building blocks[1–4]. Among these, magnetic metamaterials allow unprecedented versatility in the design of novel device architectures, exploiting the controlled propagation of the electromagnetic radiation[1], surface plasmons[5,6] and spin-waves[7–9]. In this context, the development of a new class of reprogrammable magnetic metamaterials, whose functionality can be actively redesigned on demand, would open new, far reaching directions for nanomagnetism and spintronics.

So far, the fabrication of magnetic devices through the nanopatterning of magnetic materials[10–12] has been carried out mainly using conventional lithography[10,13] or ion irradiation[11,12]. These techniques, in most cases, are irreversible and their ability to finely control the modulation of the magnetic properties within the pattern is limited. Beyond these methods, advanced scanning probe based lithography (SPL) is gaining attention in the scientific community for its flexibility and broad applicability with emerging new materials[14].

In this paper, we propose a novel, versatile approach based on SPL, namely "thermally assisted magnetic scanning probe lithography" (*tam*-SPL), to achieve a desired and reconfigurable nano-scale engineering of the magnetic properties of a continuous film. The working principle of *tam*-SPL is the local heating and cooling of an exchange-biased ferromagnetic (FM) layer by means of the hot tip of a scanning probe microscope (SPM) brought in contact with the sample, in presence of a magnetic field. This local field cooling sets a unidirectional magnetic anisotropy in the FM, due to the exchange-coupling with the adjacent antiferromagnet (AF)[15]. Phenomenologically, this causes a local pinning of the FM magnetization, which is observed as a shift in its hysteresis loop. In particular, we demonstrate the patterning of micro- and nano-structures with arbitrary shape, anisotropy and spin orientation. The pattern is stable at room temperature and cannot be permanently erased with magnetic fields, thus combining endurance and reconfigurability. These features can be exploited in the emerging field of magnonics to fabricate structures for the active manipulations of spin-waves. As a proof-of-concept experiment, we show that a local control of the spin-waves excitation and propagation can be obtained in reconfigurable magnetic tracks patterned via *tam*-SPL.

Working principle of *tam*-SPL

Magnetic patterning was performed on a Ru(2)/IrMn(7)/CoFeB(5)/SiO_2(1000)/Si (thicknesses in nm) multilayer structure, grown by magnetron sputtering, where the IrMn/CoFeB bilayer constitutes the exchange bias system. For details on the growth and magnetic characterization of the non-patterned stack, see Methods and Supplementary Information.

The working principle of *tam*-SPL is schematically illustrated in Fig.1. The exchange bias system is first initialized by heating the whole sample above the blocking temperature T_B, and subsequently cooling it in a uniform magnetic field H_i. This initialization sets a uniform unidirectional (UD) anisotropy axis in the FM film (see Fig. 1a), shifting its hysteresis loop by the exchange bias field (H_e) (see Fig. 1d and Methods for details). The hot tip of a SPM[16–20] is then used to locally heat the surface of the stack above T_B (160°C) in a uniform static magnetic field H_w = 700 Oe, which in this particular case is chosen to be opposite to the initialization field H_i. When the hot tip is displaced in its motion along the writing direction, the previously heated region of the AF film undergoes a "local field cooling" accompanied by a local rearrangement of the spins, due to the coupling with the underlying FM oriented in the direction of the external field H_w (Fig. 1b). Therefore, at the AF-FM interface in the patterned area, a different local exchange bias is established, which shifts the local hysteresis loop to the right by a new exchange bias field H_{ep} (Fig. 1e). Here, upon removal of the writing field H_w, the local remanent magnetization within the FM layer is determined by the new UD magnetic anisotropy. As a result, the spins of the FM in the patterned area (red arrows in Fig. 1c) are antiparallel to those of the surrounding film (yellow arrows) that switched back to the initial state.

Patterning capabilites

The patterning capabilities of this technique are demonstrated in Fig. 2. 20 μm-wide square pads were first defined by optical lithography in order to facilitate navigation on the sample. Then, we used *tam*-SPL to define in the pad square-, triangular- and diamond-shaped structures with different lateral sizes, from 1.5 μm to 2.5 μm (Fig. 2a), using a 3 μm/s writing speed. The SPM heater temperature (T_H) was set to 560°C, 675°C and 765°C for squares, triangles and diamonds, respectively. These T_H values ensure that the actual temperature at the tip-sample interface is well above T_B (see Supplementary Fig. 2). H_w was set antiparallel to H_i, in order to write structures with antiparallel remanent magnetization. For more details on the patterning conditions, see Methods and Supplementary Information, where a general model for the heat flow analysis developed for thermochemical (*tc*-)SPL[18] has been adapted to the present case. Figure 2a shows a magnetic force microscopy (MFM) image of a pad, taken at zero external field (remanent state) after *tam*-SPL, while Fig. 2b shows the topography of the same area. The opposite MFM magnetic contrast seen at the left and right edges of the patterns with respect to that at the pad edges demonstrates that regions with opposite UD anisotropy and remanent magnetization were written by *tam*-SPL. We remark that *tam*-SPL does not alter the morphology of the films (see Fig. 2b) and that the patterning is, therefore, "purely magnetic". A zoomed-in MFM image of the pad area is shown in Fig. 2c. Even though diamonds were written at much higher temperature than squares, the resulting magnetic contrast is the same for all patterned structures, thus indicating that once the blocking temperature of the system is exceeded, reproducible patterns can be obtained without the need of a precise control of T_H. As the degradation of exchange bias due to Mn interdiffusion starts to develop for temperatures above 350°C[21], there is a wide range of film temperatures, from 160°C to 350°C, where patterning can be performed without causing sizeable irreversibility (see Fig. 4 and related discussion). The fact that a very demanding control over the tip temperature is not required is crucial for future applications.

In order to gain a deeper understanding of the micromagnetic configuration giving rise to the magnetic contrast observed with MFM, we performed micromagnetic simulations (see

Supplementary Information) of the square, triangle and diamond patterns, as shown in Figs. 2f-h, respectively, where the black arrows indicate the orientation of the spins within the CoFeB film. The simulated out-of-plane component of the force on the ferromagnetic tip is presented in Figs. 2f-h using a blue-red (attractive-repulsive) colour code which can be associated to the dark-white contrast of MFM (see Supplementary Information for details). The agreement between simulations and experiments is very good for all patterns. It is worth noting that different kinds of 180 degrees domain wall (DW) can be engineered by controlling the pattern shape. The fine details of the DW structure for each pattern are illustrated in the simulations of Figs. 2f-i, showing that by choosing the angle of the pattern side with respect to H_i and H_w, it is possible to tune the DW magnetic configuration.

The determination of the minimum feature size achievable by performing *tam*-SPL in our multilayer system was assessed by writing single lines with H_w antiparallel to H_i and a spacing of 2 μm (see Fig. 2d). The high resolution MFM image (Fig. 2e) of the dashed area in Fig. 2d shows that the average width of a single line, measured over a 2 μm section, is 300 nm, with a minimum of 250 nm. This demonstrates that, in this condition, the minimum spacing between lines during writing allowing to keep their individuality is on the order of 300 nm. The patterned lines present two DWs of the same topology as those observed in the horizontal sides of the squares (see Fig. 2f and 2i), with magnetization antiparallel with respect to the non-patterned area. The minimum feature size and the corrugation of the lines are determined both by the domain wall width, which depends on the micromagnetic properties of the system, and by the spatial profile of the exchange bias written by *tam*-SPL. Micromagnetic simulations indicate that the width of ideal 180 degrees DWs, with the magnetization lying parallel to the wall far away from it, is in the order of 350 nm, in good agreement with the experimental width of the lines of Fig. 2e (see Supplementary Fig. 8

and ref. 22). The spatial profile of the exchange bias is given by the finite width of the thermal profile produced by the hot tip in the AF layer as well as by the spatial distribution of the blocking temperatures of the system, which reflects the distribution of grain sizes in the AF layer (see Supplementary Information). An improved spatial resolution and a reduced line corrugation can thus be achieved by optimizing the patterning conditions, the micromagnetic properties of the system[22] (e.g. the exchange bias strength, magnetocrystalline anisotropy, exchange stiffness), the grain size distribution and the thermal properties of the materials[23].

Concerning the spatial confinement of the thermal profile, it has already been demonstrated that, performing thermochemical (*tc*)-SPL on thermally insulating films[18], 15 nm features size can be achieved, which is at least comparable with state-of-the-art near-field transducers for magnetic recording technology[24]. Regarding the writing speed, note that the crucial parameter is the time required to locally heat the sample above T_B; further improvement, i.e., down to 1 μs per point-feature, could be obtained with a different thermal cantilever design[25].

In perspective, well-developed local heating technologies like those utilized in Magneto-Optical-Recording (MOR) and Heat-Assisted-Magnetic-Recording (HAMR) can be exploited for scaling up our approach [26–28].

Tunability and reconfigurability

Figure 3 shows that it is possible to finely tune the patterned magnetic anisotropy landscape by controlling the tip temperatures. In Fig. 3a, we show the MFM image taken in the remanent state from square areas patterned with T_H = 100°C, 240°C and 435°C, from the right to the left in the Figure, while applying H_w = 700 Oe antiparallel to H_i. When T_H = 100°C, the local temperature of the sample is well below the blocking temperature, therefore no magnetic contrast is seen (blue square). Correspondingly, the shift of the local hysteresis loop measured with μ-MOKE along the UD anisotropy direction (Fig. 3b), approximately -50 Oe, is comparable to the one of the loop (yellow loop in Fig. 3d) measured in the adjacent non-patterned area (yellow square in Fig. 3a). The patterned area written with T_H = 240°C (green square) shows a magnetic contrast and the corresponding local hysteresis loop (Fig. 3c) is centred at zero magnetic fields. By increasing T_H to 435°C (red square in Fig. 3a) the local hysteresis loop is eventually shifted to the right by +50 Oe (Fig. 3d), showing the full inversion of the exchange bias field. The zero shift of the loop at 240°C results from an incomplete exchange bias inversion due to the expected distribution of T_B in the film arising from the presence of grains with different size[15,29] (see Supplementary Fig. 1). This demonstrates the possibility to pattern complex magnetic anisotropy landscapes in a continuous multilayer by tuning the heater temperature during writing. Moreover, by setting H_w at different angles with respect to H_i, areas with UD anisotropy axis arbitrarily oriented with respect to the film UD anisotropy set during initialization can be patterned (see Supplementary Fig. 3).

The analysis of the magnetic behaviour of the patterned area under applied magnetic field, including the stability of the patterns, was carried out by μ-MOKE. In Fig. 3e we report some frames from a video (see Supplementary Movie 1) showing the field induced evolution of the magnetization in the patterned area of Fig. 2c (right column). The appearance and disappearance of the pattern is in agreement with the expected hysteresis loops of the patterned (non-patterned) regions, sketched in red (yellow). Furthermore, crucial for technological applications, we have verified that the same remanent state (red shapes in Fig. 3e) is always recovered even after 2000 magnetization switching cycles performed with fields up to 1000 Oe (data not shown) and that the patterns are stable 6 months after writing. Indeed, the resilience of *tam*-SPL patterns arises from the stability of exchange bias, a key property exploited also in magnetic memory applications[30–33].

This feature can be used to implement a permanent functionality, similarly to the case of magnetic devices patterned by conventional techniques, such as lithography and ion irradiation.

The reversibility of *tam*-SPL is illustrated in Fig. 4. In Fig. 4a we show a MFM image under zero external field of two squares patterned with T_H = 600°C and H_w = 700 Oe antiparallel to H_i. Figure 4b shows the very same area after local cancellation of the left square, achieved by scanning the same area with T_H = 600°C in an erasing field H_{er} = -700 Oe, opposite to H_w. The magnetic contrast almost completely disappears in the left square, while it remains unperturbed in the right one, thus indicating that the pattern was selectively erased. In addition, Fig 4c shows that it is possible to re-write the erased area with another shape, a triangle in this case, with T_H = 600°C and H_w = 700 Oe. The pattern can also be completely erased by performing a uniform field cooling, thus providing a full flexibility in writing and reversibly configuring the magnetic anisotropy landscape.

Magnonic applications

Here, we present a proof-of-concept experiment, performed by micro-focused Brillouin Light Scattering (µ-BLS), showing the potential applications of *tam*-SPL in the field of magnonics[34–38]. So far, magnonic devices were fabricated by physical patterning of magnetic thin-films[39], modulating their thickness[40] or, as in the case of bi-component magnetic devices, creating a periodic array made of two magnetic materials[41]. Here, we propose to use *tam*-SPL to pattern magnonic structures in a continuous film, thus avoiding the scattering at physical interfaces created by standard lithography and providing an easy way to introduce reconfigurability and tunability in magnonics.

The investigated sample consists of a 60 µm × 60 µm square pad, defined by optical lithography on the same multilayer structure of Fig. 2. *tam*-SPL was performed applying H_w perpendicularly to H_i for defining 2.5 μm wide tracks alternating 0° and 90° oriented remanent magnetization over a total area of 38 μm × 39 μm (orange rectangle in Fig. 5a). The MFM image of the pattern at remanence is presented in Fig. 5b, where the black arrows indicate the magnetization direction within the pattern. The sharp transition between the two different magnetization configurations is marked by well-defined and sharp 90 degrees DWs.

Coplanar wave guides (CPW), with ground to ground distance of 12 μm and oriented perpendicularly to the longitudinal direction of the *tam*-SPL tracks, were fabricated by electron-beam lithography and lift-off. μ-BLS measurements were performed in order to map the spin-waves (SWs) intensity distribution.

Fig. 5c shows the colour coded SWs intensity on a logarithmic scale measured at remanence, in the 3-5 GHz frequency range, as a function of the x-position along the CPW arms. The BLS linear scan was performed right outside the CPW, at $y = 0$ in the reference system of Fig. 5a. The orange dashed lines mark the boundaries of the tracks, while the black arrows indicate the local direction of the static magnetization, which is parallel (perpendicular) with respect to the CPW in type A (B) tracks. Remarkably, propagating SWs are efficiently excited only in type A tracks, whereas the SWs excitation efficiency is strongly reduced in type B tracks. A direct comparison of BLS spectra acquired right outside the CPW (Fig. 5e), shows that the spin-wave intensity is about 36 times higher in type A track (red circles), with respect to type B (blue squares).

Such behaviour can be explained considering that, for this CPW geometry, SWs are efficiently excited mainly by the coupling between the in-plane component of the microwave field (H_{rf} in Fig. 5a) and the corresponding component of the dynamical magnetization, associated to the SWs, while the out-of-plane component of the microwave field plays a minor role. Within the pattern, the efficiency of the coupling is high in type A and low in type B tracks, depending on whether the in-plane component of the microwave field and the corresponding component of the dynamic magnetization are parallel or perpendicular[42,43].

Fig. 5d shows the colour coded SWs intensity on a logarithmic scale acquired at remanence as a function of the distance y from the CPW, in the center of two adjacent tracks. We found that spin-waves rapidly attenuate in type B track (bottom panel), while in type A track (top panel) they efficiently propagate over a distance comparable to that observed in Py and CoFe waveguides prepared by conventional lithographic techniques[44,45]. This result is confirmed by the BLS spectra acquired at $y = 2.25$ μm in track A and B, shown in Fig. 5f. This finding can be explained taking into account that for perpendicular alignment of the SWs wavevector and the local magnetization, the SWs group velocity is much larger than for parallel alignment[46].

The above result indicates that it is possible to locally control the spin-waves excitation and propagation creating remanent magnetization patterns via *tam*-SPL. This marks the initial step for the implementation of *tam*-SPL based tunable and reconfigurable magnonic devices.

In the Supplementary Fig. 7 we discuss the design of phase shifters and magnonic crystals exploiting the modulation of the refractive index seen by the SWs in patterned regions with different relative orientation of the static magnetization and of the SWs wavevector. A single stripe can be used to implement a phase shifter to be inserted in Mach-Zehnder-type interferometers, which have been proposed as basic building blocks for computing[47]. In addition, periodic arrangement of stripes as those shown in Fig. 2d can be used to realize a magnonic crystal showing the emergence of the characteristic band-gaps. The band-width and the position of the band-gaps can be tuned by controlling the stripe width, their separation, and the width of the regions of spin rotation between the stripes. Since all these parameters can be set reversibly during patterning, our technique allows the fabrication of fully reconfigurable magnonic crystals and devices. Moreover, the active tuning of the magnonic properties after patterning can be achieved by controlling the domains extension and magnetization orientation via external magnetic fields (see Fig. 3).

Conclusions

In this work, we introduced *tam*-SPL, a straightforward, single-step method for nanopatterning reprogrammable magnetic metamaterials, leaving the film chemistry and topography unperturbed. In particular, we demonstrated the patterning of arbitrarily shaped magnetic micro- and nano-structures, with size down to 250 nm and remanent magnetization along an arbitrarily chosen direction, which are reconfigurable and stable against external magnetic perturbations. In perspective, further improvement of spatial resolution can be achieved by optimizing the patterning parameters as well as the micromagnetic properties, thermal conductivity and granularity of the magnetic multilayer. Higher patterning speed could be obtained by using arrays of many heatable cantilevers[48] or using near-field transducers, allowing for a highly localized and fast heating, with theoretical spot sizes down to 35 nm[24].

In addition, due to the extreme versatility of SPL, the magnetic patterning can be extended from continuous films to physically micro- and nano-patterned supports. Novel architectures for magnetic computing and spintronics can be envisaged, where reprogrammable magnetic metamaterials control the propagation of quasi-particles, such as domain walls in magnetic circuits, or spin-waves and surface-plasmons in magneto-plasmonic crystals. In particular, we demonstrated the local control on the spin-waves excitation and propagation in magnetic tracks patterned by *tam*-SPL. This result paves the way to the realization of reconfigurable and actively tunable devices, such as spin-wave phase shifters and filters based on magnonic crystals.

References

1. Schurig, D. *et al.* Metamaterial electromagnetic cloak at microwave frequencies. *Science* **314,** 977–80 (2006).

2. Zheludev, N. I. & Kivshar, Y. S. From metamaterials to metadevices. *Nat. Mater.* **11,** 917–24 (2012).

3. Nikitov, S. a., Tailhades, P. & Tsai, C. S. Spin waves in periodic magnetic structures—magnonic crystals. *J. Magn. Magn. Mater.* **236,** 320–330 (2001).

4. Silva, A. *et al.* Performing Mathematical Operations with Metamaterials. *Science* **343,** 160–164 (2014).

5. Temnov, V. V. Ultrafast acousto-magneto-plasmonics. *Nat. Photonics* **6,** 728–736 (2012).

6. Maccaferri, N. *et al.* Resonant Enhancement of Magneto-Optical Activity Induced by Surface Plasmon Polariton Modes Coupling in 2D Magnetoplasmonic Crystals. *ACS Photonics* **2,** 1769–1779 (2015).

7. Kobljanskyj, Y. *et al.* Nano-structured magnetic metamaterial with enhanced nonlinear properties. *Sci. Rep.* **2,** 478 (2012).

8. Lenk, B., Ulrichs, H., Garbs, F. & Münzenberg, M. The building blocks of magnonics. *Phys. Rep.* **507,** 107–136 (2011).

9. Chumak, a. V., Vasyuchka, V. I., Serga, a. a. & Hillebrands, B. Magnon spintronics. *Nat. Phys.* **11,** 453–461 (2015).

10. Monticelli, M. *et al.* On-Chip Magnetic Platform for Single-Particle Manipulation with Integrated Electrical Feedback. *Small* (2015). doi:10.1002/smll.201500916

11. Chappert, C. Planar Patterned Magnetic Media Obtained by Ion Irradiation. *Science* **280,** 1919–1922 (1998).

12. Kim, S. *et al.* Nanoscale patterning of complex magnetic nanostructures by reduction with low-energy protons. *Nat. Nanotechnol.* **7,** 567–71 (2012).

13. Ross, C. A. Patterned Magnetic Recording Media. *Annu. Rev. Mater. Res.* **31,** 203–35 (2001).

14. Garcia, R., Knoll, A. W. & Riedo, E. Advanced scanning probe lithography. *Nat. Nanotechnol.* **9,** 577–587 (2014).

15. Nogués, J. & Schuller, I. K. Exchange bias. *J. Magn. Magn. Mater.* **192,** 203–232 (1999).

16. Szoszkiewicz, R. *et al.* High-speed, sub-15 nm feature size thermochemical nanolithography. *Nano Lett.* **7,** 1064–9 (2007).

17. Wang, D. *et al.* Thermochemical Nanolithography of Multifunctional Nanotemplates for Assembling Nano-Objects. *Adv. Funct. Mater.* **19,** 3696–3702 (2009).

18. Wei, Z. *et al.* Nanoscale tunable reduction of graphene oxide for graphene electronics. *Science* **328,** 1373–6 (2010).

19. Kim, S. *et al.* Direct fabrication of arbitrary-shaped ferroelectric nanostructures on plastic, glass, and silicon substrates. *Adv. Mater.* **23,** 3786–90 (2011).

20. Pires, D. *et al.* Nanoscale three-dimensional patterning of molecular resists by scanning probes. *Science* **328,** 732–5 (2010).

21. Fernandez-Outon, L. E., Araújo Filho, M. S., Araújo, R. E., Ardisson, J. D. & Macedo, W. A. A. Setting temperature effect in polycrystalline exchange-biased IrMn/CoFe bilayers. *J. Appl. Phys.* **113,** 17D704 (2013).

22. Albisetti, E. & Petti, D. Domain wall engineering through exchange bias. *J. Magn. Magn. Mater.* **400,** 230–235 (2016).

23. Algré, E., Gaudin, G., Bsiesy, A. & Nozières, J. Improved patterned media for probe-based HAMR. *IEEE Trans. Magn.* **41,** 2857–2859 (2005).

24. Miao, L., Stoddart, P. R. & Hsiang, T. Y. Novel aluminum near field transducer and highly integrated micro-nano-optics design for heat-assisted ultra-high-density magnetic recording. *Nanotechnology* **25,** 295202 (2014).

25. King, W. P., Bhatia, B., Felts, J. R., Kim, H. J. & Kwon, B. Heated atomic force microscope cantilevers and their applications. *Annu. Rev. Heat Transf.* **XVI,** 287–326 (2013).

26. Wu, A. Q. *et al.* HAMR Areal Density Demonstration of 1 + Tbpsi on Spinstand. **49,** 779–782 (2013).

27. Saito, J., Sato, M., Matsumoto, H. & Akasaka, H. Direct Overwrite by Light Power Modulation on Magneto-Optical Multi-Layered Media. *Jpn. J. Appl. Phys.* **26,** 155–159 (1987).

28. Stanciu, C. *et al.* All-Optical Magnetic Recording with Circularly Polarized Light. *Phys. Rev. Lett.* **99,** 047601 (2007).

29. O'Grady, K., Fernandez-Outon, L. E. & Vallejo-Fernandez, G. A new paradigm for exchange bias in polycrystalline thin films. *J. Magn. Magn. Mater.* **322,** 883–899 (2010).

30. Petti, D. *et al.* Storing magnetic information in IrMn/MgO/Ta tunnel junctions via field-cooling. *Appl. Phys. Lett.* **102,** 192404 (2013).

31. Marti, X. *et al.* Room-temperature antiferromagnetic memory resistor. *Nat. Mater.* **13,** 367–374 (2014).

32. Prejbeanu, I. L. *et al.* Thermally assisted MRAMs: ultimate scalability and logic functionalities. *J. Phys. D. Appl. Phys.* **46,** 074002 (2013).

33. Papusoi, C. *et al.* Reversing exchange bias in thermally assisted magnetic random access memory cell by electric current heating pulses. *J. Appl. Phys.* **104,** 013915 (2008).

34. Camley, R. E. *et al.* High-frequency signal processing using magnetic layered structures. *J. Magn. Magn. Mater.* **321,** 2048–2054 (2009).

35. Kim, S.-K., Lee, K.-S. & Han, D.-S. A gigahertz-range spin-wave filter composed of width-modulated nanostrip magnonic-crystal waveguides. *Appl. Phys. Lett.* **95,** 082507 (2009).

36. Chumak, A. V, Serga, A. a & Hillebrands, B. Magnon transistor for all-magnon data processing. *Nat. Commun.* **5,** 4700 (2014).

37. Krawczyk, M. & Grundler, D. Review and prospects of magnonic crystals and devices with reprogrammable band structure. *J. Phys. Condens. Matter* **26,** 123202 (2014).

38. Csaba, G., Papp, a. & Porod, W. Spin-wave based realization of optical computing primitives. *J. Appl. Phys.* **115,** 17C741 (2014).

39. Neusser, S. & Grundler, D. Magnonics: Spin Waves on the Nanoscale. *Adv. Mater.* **21,** 2927–2932 (2009).

40. Gubbiotti, G. *et al.* Collective spin waves on a nanowire array with step-modulated thickness. *J. Phys. D. Appl. Phys.* **47,** 105003 (2014).

41. Tacchi, S. *et al.* Forbidden band gaps in the spin-wave spectrum of a two-dimensional bicomponent magnonic crystal. *Phys. Rev. Lett.* **109,** 1–5 (2012).

42. Kalinikos, B. a. Excitation of propagating spin waves in ferromagnetic films. *IEE Proc. H Microwaves, Opt. Antennas* **127,** 4 (1980).

43. Brächer, T. *et al.* Generation of propagating backward volume spin waves by phase-sensitive mode conversion in two-dimensional microstructures. *Appl. Phys. Lett.* **102,** 2011–2016 (2013).

44. Vogt, K. *et al.* Realization of a spin-wave multiplexer. *Nat. Commun.* **5,** 3727 (2014).

45. Urazhdin, S. *et al.* Nanomagnonic devices based on the spin-transfer torque. *Nat. Nanotechnol.* **9,** 509–13 (2014).

46. Stancil, D. D. & Prabhakar, A. *Spin Waves Theory and Applications*. (Springer New York, 2009).

47. Schneider, T. *et al.* Realization of spin-wave logic gates. *Appl. Phys. Lett.* **92,** 022505 (2008).

48. Carroll, K. M. *et al.* Parallelization of thermochemical nanolithography. *Nanoscale* **6,** 1299–1304 (2014).

49. Nikulina, E., Idigoras, O., Vavassori, P., Chuvilin, A. & Berger, A. Magneto-optical magnetometry of individual 30 nm cobalt nanowires grown by electron beam induced

deposition. *Appl. Phys. Lett.* **100,** 142401 (2012).

50. Madami, M., Gubbiotti, G., Tacchi, S. & Carlotti, G. in *Solid State Physics, vol.63* (ed. Stamps, R. E. C. and R. L.) 79–150 (Burlington: Academic Press, 2012).

Acknowledgements

E.A. thanks Keith Carroll, Lu Xi for fruitful discussion and Paolo Sarti for the inspiring talks. M.M. and S.T. thank Giovanni Carlotti for the helpful discussion. E.A. and E.R. acknowledge the support of the Office of Basic Energy Sciences of the US Department of Energy (DE-FG02-06ER46293). E.R. acknowledges partial support of the National Science Foundation (NSF) grant CMMI 1436375. E.A., D.P. and R.B. acknowledge support from the Cariplo project UMANA (Project No. 2013-0735). R.B. and D.P. acknowledges support from the Cariplo project MAGISTER (Project No. 2013-0726). M.M. and S.T acknowledge support from the Ministero Italiano dell'Università e della Ricerca (MIUR) under the PRIN2010 project (No. 2010ECA8P3). M.P. and P.V. acknowledge support from the Basque Government (Program No. PI_2015_1_19) and (M.P.) from the Spanish Ministry of Economy Competitiveness through the grant BES-2013-063690. This work was partially performed at Polifab, the micro- and nano-technology center of the Politecnico di Milano.

Authors contribution

E.A. conceived and designed the experiments with the help of D.P.. E.R. and R.B. coordinated and supervised the research work. E.A. performed the patterning experiments, MFM characterization and simulations. D.P. fabricated the samples. W.P.K. provided the thermal SPM tips. E.A., M.P., P.V. and R.B. performed the MOKE characterization. E.A and D.P fabricated the samples for μ–BLS measurements. M.M. and S.T. performed the μ–BLS measurements. A.P., G.C., W.P. performed the simulation of the magnonic structures. E.A., D.P., M.M., S.T., P.V., E.R. and R.B. wrote the manuscript. All the authors contributed to discussions regarding the research.

Competing Financial Interest

The authors declare no competing financial interests.

Additional Information

Supplementary information accompanies this paper at www.nature.com/naturenanotechnology. Reprints and permission information is available online at http://npg.nature.com/reprintsandpermissions/. Correspondence and requests for materials should be addressed to E.A., E.R., R.B.

Figure Captions

Figure 1. Magnetic patterning via *tam*-SPL. a, After initialization, the magnetization of the ferromagnetic layer (yellow arrows) is uniformly pinned in one direction by the exchange interaction with the antiferromagnetic layer (blue arrows). **b,** Sweeping a heated SPM tip on the sample surface in presence of an external magnetic field H_w produces a "local field-cooling" in the antiferromagnet (green arrows), which re-sets the exchange bias direction according to the underlying CoFeB spins (red arrows), aligned with H_w. **c,** When the external magnetic field H_w is removed, the magnetic domain configuration in the ferromagnet is stabilized by the local

exchange bias. The bottom panels show the magnetic hysteresis loops before **d,** and after patterning **e,**. H_e and H_{ep} indicate the opposite shift in the loops due to the exchange bias in the non-patterned and patterned areas, respectively.

Figure 2. Magnetic Force Microscope characterization and micromagnetic simulations of the patterned domain structures. MFM image **a**, and topography **b**, of the same pad after performing *tam*-SPL. The patterned domains are clearly visible in the MFM image, whereas no change in the surface topography is observed. **c,** zoomed-in MFM image of square- (top row), triangular- (center row) and diamond- (bottom row) shaped magnetic domains with size 2.5 μm (right column), 2 μm (center column) and 1.5 μm (left column). The magnetic contrast marks the domain boundaries. **d,** MFM of single lines 12 μm long. **e,** High-resolution MFM image of the dashed rectangle in **d,** showing a minimum width of 250 nm. All MFM images are acquired under no external magnetic field. **f-i,** Micromagnetic simulation of the magnetic configuration of the patterned domains. The arrows indicate the direction of the spins, the color map is the normalized magnetic force acting on the MFM tip. The bottom panels show a zoomed view of the domain walls. In square structures **f**, head-to-head and tail-to-tail DWs are defined on the left and right sides respectively, with the spins within the DW aligned along the wall. A different micromagnetic configuration is observed on the top and bottom sides, where the DW spins are perpendicular to the wall. In the triangle and diamond shapes **g-h**, the arrangement of the spins within the wall is in between the two cases described above. Scale bars, 4 μm in **a-b**, 2 μm in **c-d**, 1 μm in **f-g-h**, 500 nm in **e**, 250 nm in **i**.

Figure 3. Tunability of the magnetic anisotropies and evolution of the patterned domains with the external magnetic field. a, MFM image at zero magnetic field from a non-patterned area

(yellow square) and from areas patterned with T_H = 100°C (blue square), 240°C (green square) and 435°C (red square) and H_w = 700 Oe. **b,c,d,** μ-MOKE hysteresis loop corresponding to the blue, green, red and yellow squares of **a**, respectively. Starting from the initialized sample (yellow loop, H_e = -50 Oe), by increasing the heater temperature, it is possible to tune the magnetic anisotropy and hence the exchange bias field (from H_{ep} = -50 Oe, blue loop until H_{ep} = +50 Oe, red loop). **e,** μ-MOKE frames from a video acquired while sweeping a magnetic field parallel to the UD anisotropy axis, from -100 Oe to +100 Oe (top sequence) and from +100 Oe to -100 Oe (bottom sequence). At the beginning of the top sequence, the magnetization of both patterned and non-patterned areas lies in the negative direction (dark contrast); at around -20 Oe the magnetization of the non-patterned film switches giving rise to a bright contrast, while the patterned areas remain dark. The dark contrast eventually disappears at about +50 Oe, when the switching takes place also in the patterned areas. An analogue switching behaviour is observed in the bottom sequence.

In the center, the hysteresis loops from the non-patterned (yellow) and patterned (red) areas are sketched and the switching fields are marked. Scale bars, 2 μm in **a** and **e**.

Figure 4. Writing-erasing-rewriting capability. a, MFM image of two squares patterned with T_H = 600°C and H_w = 700 Oe. **b,** The very same area after the erasure of the left square obtained by scanning it with T_H = 600°C and an erasing field H_{er} = -700 Oe, opposite to H_w and in the same direction of the initializing field H_i. **c,** A triangle is then re-written on the left area with T_H = 470°C and H_w = 700 Oe. Note that both the erasure and the rewriting processes leave the right square unaffected. Scale bar, 2 μm.

Figure 5. Patterning magnonic structures. a, Optical image of the sample, showing the coplanar waveguide (CPW) generating the Oersted field H_{rf} and the pad where the *tam*-SPL patterning was

performed. The orange rectangle marks the patterned area. Scale bar: 4 μm. **b,** MFM image of the magnonic structures, consisting of 2.5 μm wide tracks with alternated 0° and 90° oriented remanent static magnetization (black arrows). The track boundaries are marked by dashed lines in panel **a**. Scale bar: 4 μm. **c,** One-dimensional map of the spin-wave intensity measured at remanence by μ-BLS along the *x*-direction (with a 0.5 μm step size), right outside the CPW. Spin-waves are efficiently excited within tracks of type A. **d,** One-dimensional map of the spin-wave intensity measured at remanence by μ-BLS as a function of the distance *y* from the CPW (with a 0.25 μm step size). **e-f,** Spin-wave spectra measured in track A (red circles) and track B (blue squares) at a distance $y = 0$ μm and $y = 2.25$ μm from the CPW, respectively.

Methods

Sample fabrication and characterization

$Co_{40}Fe_{40}B_{20}$(5 nm)/$Ir_{22}Mn_{78}$(7 nm)/Ru(2 nm) stacks were deposited on Si/SiO_2(1000 nm) substrates by DC magnetron sputtering using an AJA Orion8 system with a base pressure below 1×10^{-8} Torr. During the deposition, a 300 Oe magnetic field (H_G) was applied in the sample plane for setting the magnetocrystalline uniaxial (UA) anisotropy direction in the CoFeB layer and the exchange bias direction in the as-grown sample. Both the critical temperature at which the exchange bias disappears (blocking temperature T_B) and the exchange bias strength decrease with the antiferromagnetic layer (IrMn) thickness. We used a 7 nm IrMn layer, as this thickness ensures both a strong exchange bias and a T_B above room temperature (160°C, as shown in Supplementary Fig. 1), allowing to perform local field cooling by scanning the heatable SPM tip. Concerning the

FM, the 5 nm CoFeB thickness ensures both a sizeable exchange bias, which decreases for higher FM thickness[15], and a straightforward characterization of the magnetic domains by magnetic force microscopy (MFM) and magneto-optical Kerr effect microscopy (μ-MOKE). The multilayer surface roughness measured in a 1 μm^2 area is 0.15 nm rms. Squared pads with a 400 μm^2 area were microfabricated by optical lithography and ion milling, allowing for the individuation of the magnetic patterns defined by *tam*-SPL. After microfabrication, in order to set a unidirectional (UD) anisotropy axis in the CoFeB film, the samples underwent a field cooling starting from 220°C (above the blocking temperature T_B) in vacuum and in a 4000 Oe magnetic field H_i applied along the UA axis of the CoFeB film. The magnetic characterization of the stacks was performed in a Microsense Vibrating Sample Magnetometer equipped with a heater for temperature dependent measurements.

***tam*-SPL**

Thermally assisted magnetic scanning probe lithography was performed with a modified Agilent 5500 SPM system equipped with custom made silicon SPM cantilevers integrated with a Joule-heating resistive heater[17,18,25]. Details about these thermal cantilevers and temperature calibration are reported in Supplementary Information. A National Instruments® NI cDAQ-9178 was used for controlling and recording the current passing through the cantilever to achieve joule heating. In order to pattern arbitrary one or two dimensional geometries, such as lines, polygons and complex planar shapes, we used MATLAB® scripts in combination with the Agilent PicoView software. The magnetic patterns were written by raster-scanning the heated tip in contact mode using a linear speed of 3 μm/s. Two permanent magnets were employed for generating the uniform

700 Oe external magnetic field applied in the sample plane during patterning. An arbitrary angle between the direction of the external field and the initialization direction of the sample was set by physically rotating the sample with respect to the magnets.

MFM characterization

Magnetic force microscopy characterization of the patterned magnetic domains was performed with the same Agilent 5500 SPM system used for *tam*-SPL, equipped with a Nanosensors PPP-MFMR AFM magnetic probe. MFM imaging was performed in lift-mode, with lift-heights of 100 nm (Fig.2a-c-d, Fig. 3a, Fig. 4, Fig. 5b in the main text and Supplementary Figs. 3 and 4) and 30 nm (Fig. 2e).

Micro-MOKE characterization

In order to conduct investigations of the magnetization distribution at the sub-micrometer length scale we used a characterization tool based on magneto-optic Kerr effect imaging/magnetometry based on an optical wide-field polarization microscope optimized for Kerr microscopy (Evico Gmbh). Arbitrary magnetic fields can be applied during observation so that domain nucleation and magnetization processes can be observed. Indeed, the domain contrast in the image is directly sensitive to the projection of the magnetization along the sensitivity direction, which is set either parallel or perpendicular to the externally applied field. To this purpose, the microscope was equipped with a rotatable bipolar electromagnet that allows the application of a magnetic field of intensity up to 5000 Oe along an arbitrary direction in the sample plane. Two different operational modes of the microscope were used: in the first, through a high sensitivity and resolution CCD camera, magnetic contrast imaging of the sample surface was performed with a spatial resolution ~ 500 nm. In the second, the CCD camera was used as a conventional photodetector to measure the local magnetization reversal (hysteresis loops) by selecting an arbitrary region of interest (ROI) and thus a limited number of pixel. At maximum optical magnification (objective 100x followed by a 4x tube lens), each CCD pixel corresponds to an area of 15 x 15 nm^2 of the sample surface. Single shot hysteresis loops of sample surface portions as small as 1 x 1 μm^2 were measured[49].

BLS microscopy measurements

μ-BLS measurements were performed focusing about 5 mW of monochromatic light, from a Diode-Pumped-Solid-State (DPSS) laser operating in the spectral line of 532 nm, with a microscope dark-field objective of large numerical aperture (NA = 0.75) and super-long working distance (4.7 mm)[50].

Using the same objective, a coaxial viewing system based on a collimated LED light source (455 nm wavelength), a beam expander and a CCD camera is implemented into the setup, to obtain a direct visualization of the laser spot and of the sample region under investigation. Electrical access to the sample is achieved thanks to a specially designed ground-signal-ground (GSG) antenna with large extended pads where a DC is injected with a picoprobe.

During μ-BLS measurements the sample holder and the BLS spectrometer are controlled by the TFPDAS4-MICRO and TFPDAS4 software, developed at Kaiserslautern University, which provides an active stabilization of the lateral and vertical position of the sample with a precision of about 50 nm.

References for the methods

15. Nogués, J. & Schuller, I. K. Exchange bias. *J. Magn. Magn. Mater.* **192,** 203–232 (1999).

17. Wang, D. *et al.* Thermochemical Nanolithography of Multifunctional Nanotemplates for Assembling Nano-Objects. *Adv. Funct. Mater.* **19,** 3696–3702 (2009).

18. Wei, Z. *et al.* Nanoscale tunable reduction of graphene oxide for graphene electronics. *Science* **328,** 1373–6 (2010).

25. King, W. P., Bhatia, B., Felts, J. R., Kim, H. J. & Kwon, B. Heated atomic force microscope cantilevers and their applications. *Annu. Rev. Heat Transf.* **XVI,** 287–326 (2013).

49. Nikulina, E., Idigoras, O., Vavassori, P., Chuvilin, A. & Berger, A. Magneto-optical magnetometry of individual 30 nm cobalt nanowires grown by electron beam induced deposition. *Appl. Phys. Lett.* **100,** 142401 (2012).

50. Madami, M., Gubbiotti, G., Tacchi, S. & Carlotti, G. in *Solid State Physics, vol.63* (ed. Stamps, R. E. C. and R. L.) 79–150 (Burlington: Academic Press, 2012).

Figure 1

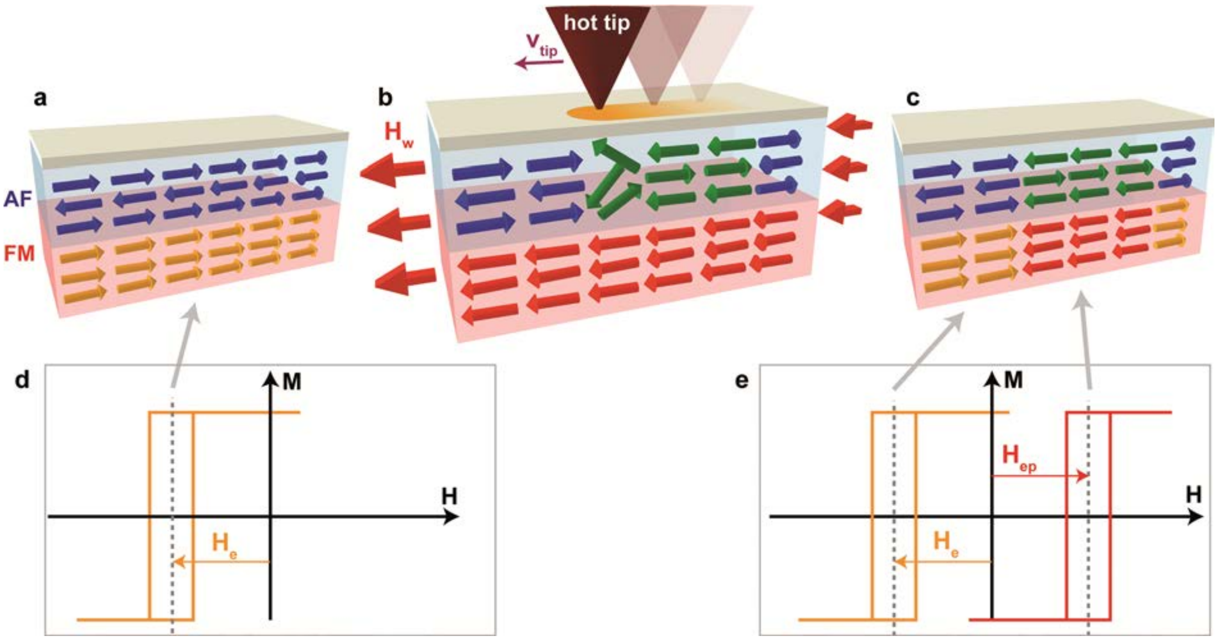

Figure 2

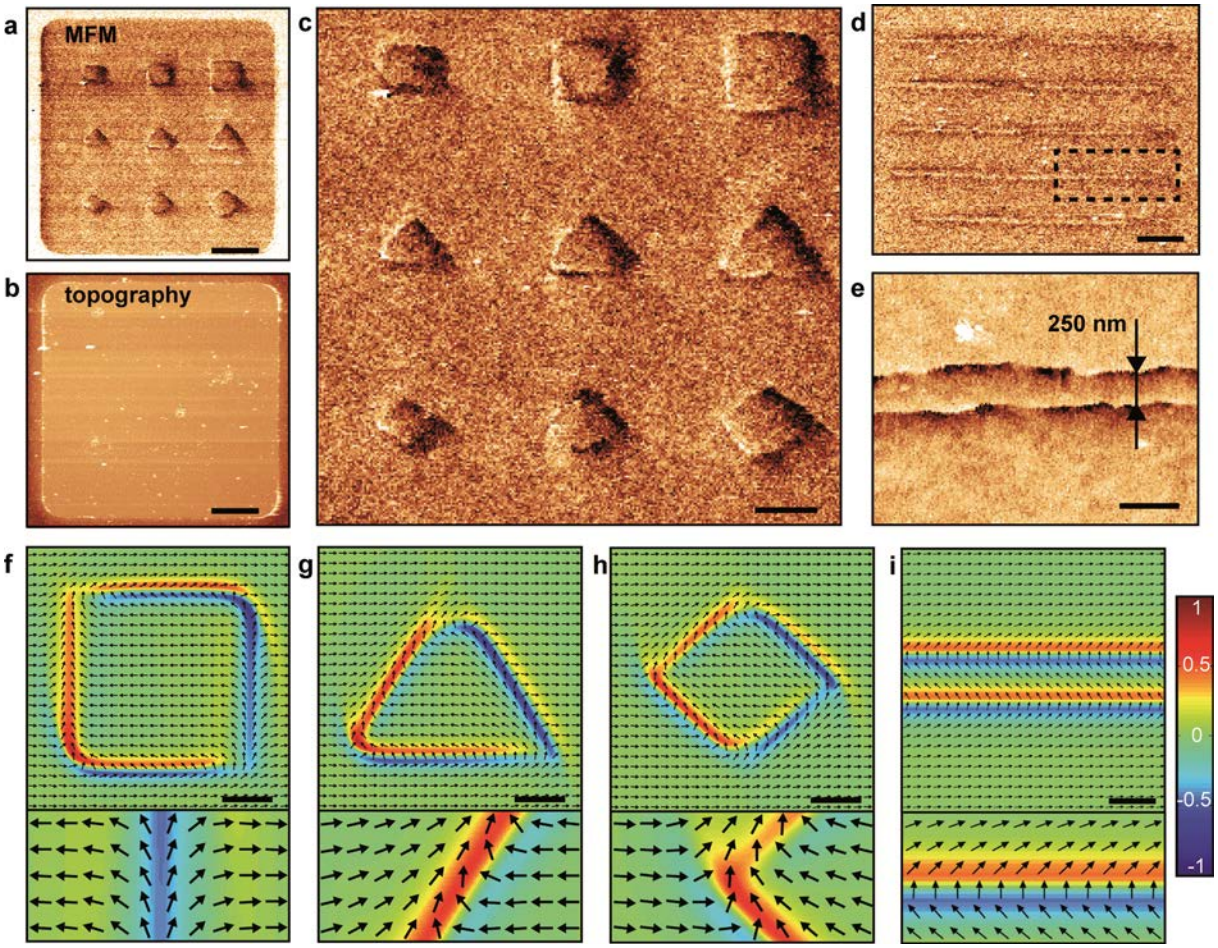

Figure 3

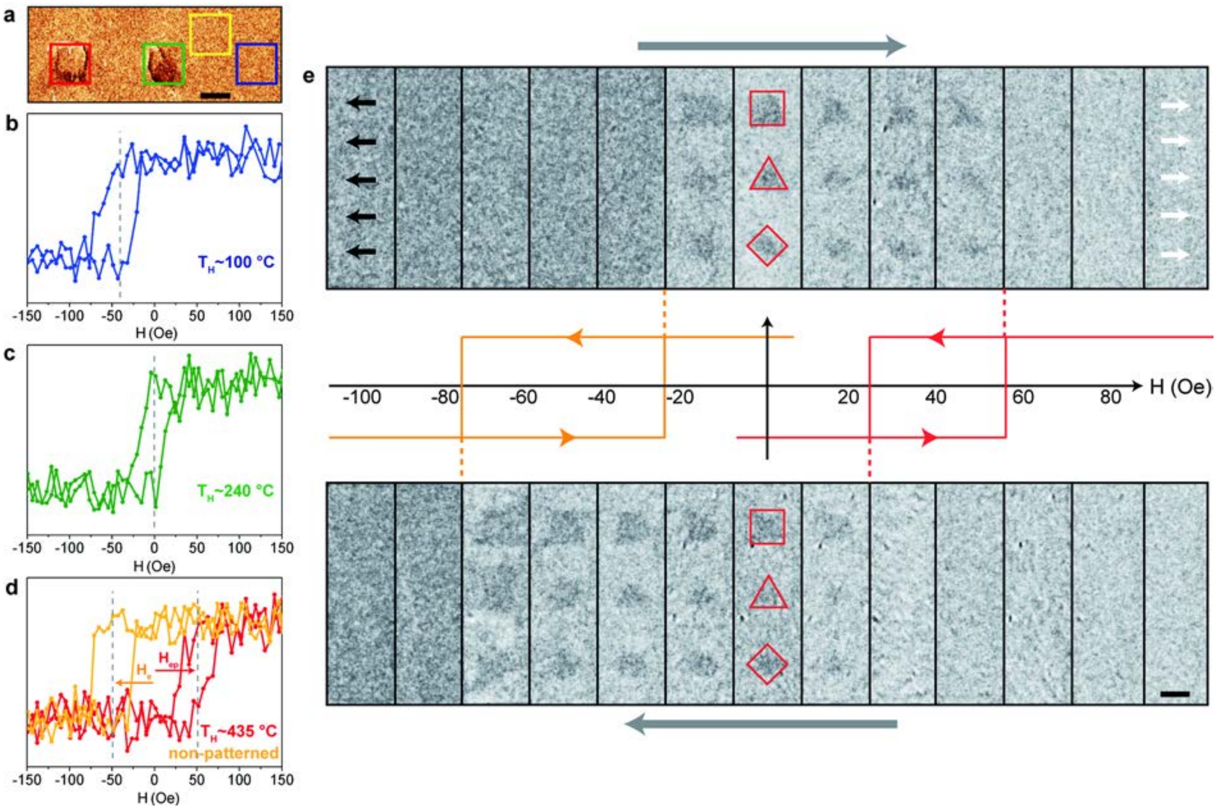

Figure 4

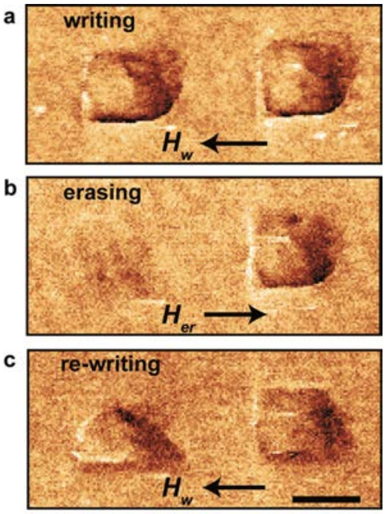

Figure 5

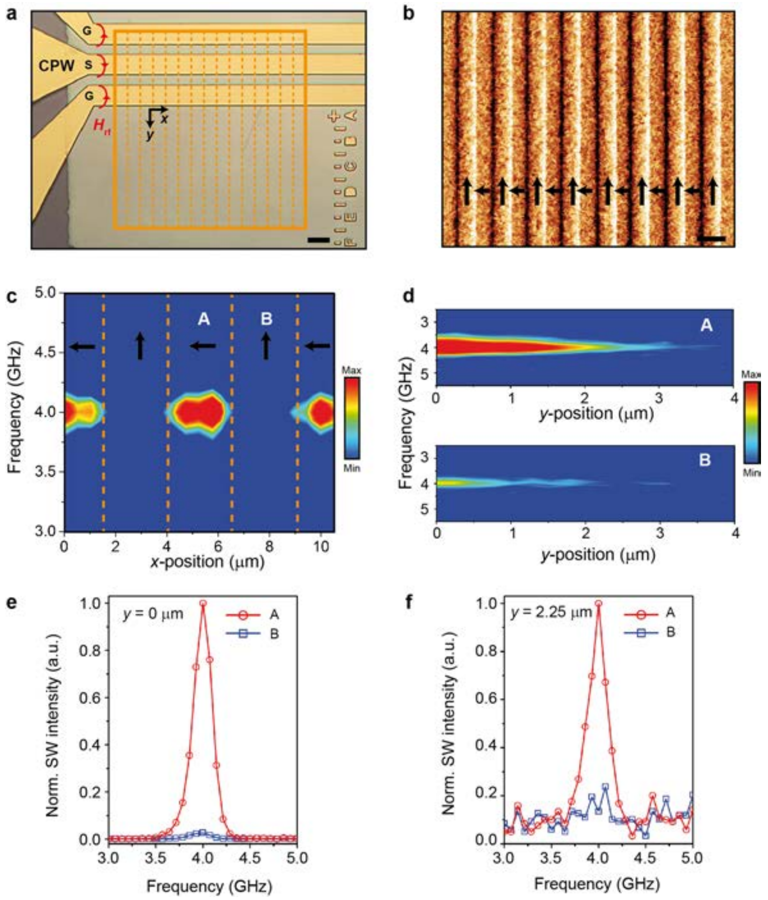
a
G
CPW
S
G
H_n
x
y
b
c
Frequency (GHz)
5.0
4.5
4.0
3.5
3.0
A
B
Max
Min
0
2
4
6
8
10
x-position (μm)
d
A
B
Frequency (GHz)
3
4
5
0
1
2
3
4
y-position (μm)
Max
Min
e
Norm. SW intensity (a.u.)
y = 0 μm
A
B
Frequency (GHz)
3.0
3.5
4.0
4.5
5.0
0.0
0.2
0.4
0.6
0.8
1.0
f
y = 2.25 μm
A
B
Norm. SW intensity (a.u.)
Frequency (GHz)